J. Fluid Mech. (1985), *vol.* 151, *pp.* 311–335
Printed in Great Britain

A performance-prediction theory for partially submerged ventilated propellers

By OKITSUGU FURUYA

Tetra Tech, Inc., 630 North Rosemead Boulevard, Pasadena, California 91107

(Received 6 February 1984 and in revised form 23 April 1984)

A partially submerged propeller theory was developed by employing a singularity distribution method. Unsteady pressure doublets and pressure sources represented the blade camber and blade-and-cavity thickness respectively. The induced velocities were derived by reducing the formula to a lifting-line configuration. The free-surface effect was considered by use of the image method. The induced velocities contained the singular integrals of 5th order, which are usually numerical unstable. An effort was made to derive numerically stable formulae from these singular equations by applying a method similar to the induction-factor method of Morgan & Wrench (1965) and Lerbs (1952) used for steady-state fully wetted propeller problems. These new formulae are not only applicable to the present partially submerged ventilated propeller problem, but also to general unsteady subcavitating and cavitating propeller problems such as propeller starting-up and non-periodic loading problems. By combining the two-dimensional water entry-and-exit theory of Wang (1979), the thrust and torque coefficients were calculated for representative partially submerged propellers and favourably compared with the experimental data.

1. Introduction

In recent years partially submerged air-ventilated propellers have attracted growing attention as efficient thrusting devices for high speed sea craft. Potentially, this type of propeller provides a better performance than fully submerged supercavitating propellers. This seems attributable to the following two major factors:

(i) reduction of the hydrodynamic resistance for the appendages such as shafts, struts, etc., which would support the propeller in water; and

(ii) reduction of the adverse cascade effect by providing the free surface for air ventilation.

The origin of the partially submerged propeller goes back to the late 19th century, and many such propellers have been tested with different types of boats since then. (Hadler & Hecker (1968) summarized its history in their report.) Most of the development conducted for the propeller was, however, on a trial-and-error basis and until recently no theoretical foundation existed for improvement of the partially submerged propeller performance. The pioneer work in this subject was provided by Yim (1969, 1971, 1974) who developed the theory for the hydrodynamic entry-and-exit characteristics of the thin foil and symmetric wedge with ventilation. The method applied there assumed the two-dimensional flow field by unfolding the cylindrical plane which is the rotational path of a blade at a certain radius. The problem to be solved was therefore that of an unsteady blade motion going in (entry) and out (exit) of this water layer. Using a similar two-dimensional assumption, Wang (1977, 1979) recently solved a rather complete water entry-and-exit problem including such

features as general nonsymmetric blade profile, ventilation and oblique entry-and-exit. This facilitated a convenient and powerful tool for determining the two-dimensional sectional loading for practical blade profiles at various entry and exit angles.

All the theoretical works conducted so far were based on the two-dimensional assumptions and, to the best of our knowledge, there is no three-dimensional theory for partially submerged propellers with ventilation. The preliminary work for this problem was conducted by the author who incorporated various three-dimensional effects such as propeller configurations and presence of a free surface. The unsteady propeller theory developed there used a linearized approximation for velocities and thus could solve a linearized equation of motion for a potential function Φ. This function Φ was then determined by distributing the pressure doublets and pressure sources which represented the blade camber and blade-and-cavity thickness, respectively. The induced velocities were then derived by taking the derivatives of Φ. Up to this point the theory was developed as a lifting-surface theory. However, for simplicity, this lifting-surface expression was reduced to that of lifting line by shrinking the propeller chord to a single line with the total amount of loading lift remaining the same. In order to represent the free-surface effect for propeller performance, the image method was applied. For the image of pressure doublet, that of the same strength and sign was distributed, whereas, for the image of pressure source, that of the same strength but with negative sign was distributed, both on the location of the mirror image with respect to a free surface.

The induced velocities obtained there included the integrals of the fifth-order singularities. A singular integral method of Hadamard (see the report by Mangler (1951) for its detailed treatment) was employed to avoid the numerical instabilities, but resulted in only partial success. As the numerical control points along the span direction increased, first the results showed a trend of convergence but then started diverging as the number of points further increased. Although the solutions of intermediate convergence were presented and compared with the experimental data of Hadler and Hecker, the accuracy of these solutions was uncertain.

The objective of the present work was, therefore, to improve the accuracy of the theory by resolving the numerical instabilities encountered in the previous work. In order to avoid these numerical instabilities, instead of finding other numerical integral methods, better mathematical formulae for calculating the induced velocities were sought. It means that effort has been made to convert the integrals having the fifth-order singularities into those of the third-order singularities. This type of conversion is typical in the steady-state lifting-line theory but had not been done for the unsteady problem. The conversion has been successfully done here and the numerical stability and accuracy are then guaranteed by using the concept of induction factors similar to that of Lerbs (1952) and Morgan & Wrench (1965).

In the following the mathematical formulation, solution method and numerical analysis will be described in detail, followed by some representative results of computations obtained with the present theory. Although many experiments have been conducted to date regarding the partially submerged propeller, they are not readily available. We have thus chosen the experimental data of Hadler & Hecker (1968), which existed in the open literature, for comparison.

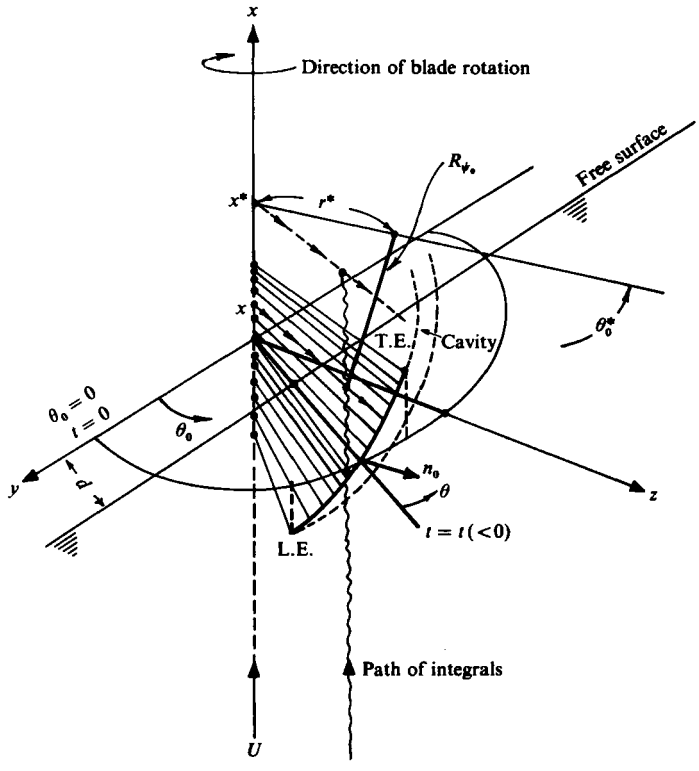

FIGURE 1. A schematic diagram for propeller flow configuration in which the propeller rotates at a fixed position while the flow approaches with the uniform velocity U.

2. Mathematical formulation

2.1. *Basic equations*

Figure 1 shows a schematic diagram of a partially submerged propeller blade rotating around the x-axis in the uniform flow of velocity U approaching from the negative infinity of x. This type of flow model is similar to that used by Cox (1968) who developed the theory for supercavitating propellers. The propeller shaft line represented by the x-axis is placed in the air domain, a distance of d from the free-surface boundary. The cylindrical coordinate system (x, r, θ) will be used throughout the present analysis with no subscripts for the coordinate θ fixed on the blade and with subscripts 0 for the inertial coordinate θ. The time is measured when the centreline component of the blade helical plane is at $\theta_0 = 0$ so that the time corresponding to that of figure 1 is interpreted as of negative value. It means that the event of propeller rotation started at some negative time. In order to identify the quantities related to the blade singularities from those of interest we will use superscripts $*$ for the latter.

In the present analysis an unsteady linearized theory with inviscid and no-gravity assumptions is employed. The velocity components in the x, r, θ_0 directions are written as $(U+u_{x^*}, u_{r^*}, u_{\theta_0^*})$. Defining the perturbed velocity quantities $(u_{x^*}, u_{r^*}, u_{\theta_0^*})$ by $\boldsymbol{u}$, one can write a linearized equation of motion:

$$\frac{\partial \boldsymbol{u}}{\partial t} + U\frac{\partial \boldsymbol{u}}{\partial x^*} = -\nabla\frac{\hat{p}}{\rho},$$

which can be expressed in terms of a velocity potential Φ:

$$\frac{\partial \Phi}{\partial t}+U\frac{\partial \Phi}{\partial x^*}=-\frac{\hat{p}}{\rho}, \tag{1}$$

where

$$\boldsymbol{u}=\nabla^*\Phi, \tag{2}$$

and $\hat{p}$ is the static pressure of the fluid. Solving (1) for Φ gives:

$$\Phi(x^*, r^*, \theta_0^*; t)=-\frac{1}{U}\int_{-\infty}^{x^*-x}\frac{\hat{p}}{\rho}\left(\nu+x, r^*, \theta_0^*, t-\frac{x^*-(\nu+x)}{U}\right)\mathrm{d}\nu, \tag{3}$$

where the boundary condition $p=0$ at $x^*=-\infty$ has been used. Applying the continuity equation $\operatorname{div}\boldsymbol{u}=0$ to (1) and (2), we obtain the Laplace equation for $\hat{p}$:

$$\nabla^{*2}\hat{p}=0.$$

Green's theorem will be used for $\hat{p}$ which satisfies the above Laplace equation so that the solution for $\hat{p}$ can be expressed:

$$\hat{p}(x^*, r^*, \theta_0^*; t)=p+\not{p}, \tag{4}$$

where

$p(x^*, r^*, \theta_0^*; t) \equiv$ pressure due to the real blade (pressure doublet term) and cavity (pressure source term)

$$=-\frac{1}{4\pi}\sum_k\left\{\iint_{S_b}\Delta p(x, r, \theta; t)\frac{\partial}{\partial n_0}\left(\frac{1}{R_{\Psi_0}}\right)\mathrm{d}S - \iint_{S_b+S_c}\frac{1}{R_{\Psi_0}}\Delta\left\{\frac{\partial}{\partial n_0}[p(x, r, \theta; t)]\right\}\mathrm{d}S\right\}, \tag{5}$$

$\not{p}(x^*, r^*, \theta_0^*; t) \equiv$ pressure due to the image blade and cavity

$$=-\frac{1}{4\pi}\sum_k\left\{\iint_{\mathscr{S}_b}\Delta p(x, r, \theta; t)\frac{\partial}{\partial n_0}\left(\frac{1}{\mathscr{R}_{\Psi_0}}\right)\mathrm{d}S + \iint_{\mathscr{S}_b+\mathscr{S}_c}\frac{1}{\mathscr{R}_{\Psi_0}}\Delta\left\{\frac{\partial}{\partial n_0}[p(x, r, \theta; t)]\right\}\mathrm{d}S\right\}, \tag{6}$$

$$\Delta p \equiv p^+-p^-,$$

$$\Delta\left\{\frac{\partial}{\partial n}p\right\} \equiv \left(\frac{\partial p}{\partial n}\right)^+-\left(\frac{\partial p}{\partial n}\right)^-,$$

$n \equiv$ normal to linearized surface, positive from pressure side to suction side,

$$R_{\Psi_0} \equiv [(x^*-x)^2+r^2+r^{*2}-2rr^*\cos\Psi_0]^{\frac{1}{2}},$$

$$\Psi_0 \equiv \theta_0-\theta_0^*+\sigma_k,$$

$$\theta_0 \equiv \theta-\omega t,$$

$$\sigma_k \equiv \frac{2\pi}{K}(k-1),$$

$K \equiv$ number of blades

$S \equiv$ moving surface consisting of propeller blade surface S_b and cavity surface S_c,

$S_b, S_c \equiv$ propeller blade and cavity surfaces, respectively, where, to satisfy the zero-pressure condition on the free surface, the image part $\not$ has been added in (4) with the pressure doublet term of the same sign and the pressure source of the opposite sign. Detailed derivations of the image part will be treated separately later.

The detailed description for the image part will be provided later.

The moving blade surface S is considered to be composed of helical lines of varying pitch in the r-direction;

$$S: \quad x-\theta R\lambda(r)=0, \quad \lambda = U(r)/\omega R,$$

where λ denotes advance coefficient as a function of r. It must be mentioned now that the theory developed here will be applied to the wake-adapted field by varying λ as a function of r as is seen above. By using the gradient components of this helical plane, one can write the directional derivative $\partial/\partial n_0$ as follows:

$$\frac{\partial}{\partial n_0} = -\frac{r\dfrac{\partial}{\partial x} - r(\theta_0+\omega t)\,R\lambda_r \dfrac{\partial}{\partial r} - \dfrac{R\lambda}{r}\dfrac{\partial}{\partial \theta_0}}{[r^2+(R\lambda)^2+(r(\theta_0+\omega t)\,R\lambda_r)^2]^{\frac{1}{2}}}, \tag{7}$$

where $\lambda_r \equiv \mathrm{d}\lambda/\mathrm{d}r$. Thus

$$\frac{\partial}{\partial n_0}\left(\frac{1}{R_{\Psi_0}}\right) = -\frac{r(x^*-x)+R\lambda r^*\sin\Psi_0 - r(\theta_0+\omega t)\,R\lambda_r(r-r^*\cos\Psi_0)}{[r^2+(R\lambda)^2+\{r(\theta_0+\omega t)\,R\lambda_r\}^2]^{\frac{1}{2}}R^3_{\Psi_0}} \tag{8}$$

and

$$\mathrm{d}S = [r^2+(R\lambda)^2+\{r(\theta_0+\omega t)\,R\lambda_r\}^2]^{\frac{1}{2}}\,\mathrm{d}\theta\,\mathrm{d}r. \tag{9}$$

In order to derive a simplified first-cut method of partially submerged propeller theory we take only the doublet effects for the present analysis, neglecting the source effects, i.e. the cavity-thickness effects on the induced flow velocities. Therefore substitution of (8) and (9) into (5) yields

$$p(\nu+x, r^*, \theta_0^*; \tau) = \frac{1}{4\pi}\sum_k \int_{r_f(\tau)}^{R}\int_{\theta_L}^{\theta_T} \Delta p(r,\theta,\tau)\frac{N_\nu}{R_\nu^3}\,\mathrm{d}r\,\mathrm{d}\theta, \tag{10}$$

where

$$\tau = t - \frac{x^*-(\nu+x)}{U}, \tag{11}$$

$$\Psi_\nu = \theta - \omega\tau - \theta_0^* + \sigma_k, \tag{12}$$

$$N_\nu = r\nu + R\lambda r^*\sin\Psi_\nu - r(\theta_0+\omega\tau)\,R\lambda_r(r-r^*\cos\Psi_\nu), \tag{13}$$

$$R_\nu = [\nu^2+r^2+r^{*2}-2rr^*\cos\Psi_\nu]^{\frac{1}{2}}, \tag{14}$$

$\theta_L, \theta_T \equiv$ angular coordinates of the blade leading and trailing edges, respectively,

$r_f, R \equiv$ radial coordinates defining the radial distances at the free surface and tip measured from the centre of shaft, respectively.

Substituting (10) into (3), one obtains

$$\Phi(x^*, r^*, \theta_0^*; t) = -\frac{1}{4\pi U}\sum_k \int_{-\infty}^{x^*-x}\mathrm{d}\nu \int_{r_f(\tau(\nu))}^{R}\mathrm{d}r \int_{\theta_L}^{\theta_T}\frac{1}{\rho}\,\Delta p(r,\theta,\tau(\nu))\frac{N_\nu}{R_\nu^3}\,\mathrm{d}\theta. \tag{15}$$

A further simplification of the problem is made by representing each of the submerged blades as a lifting line so that one can define the dipole-like singularity

$$\int_{\theta_L}^{\theta_T} \frac{1}{\rho} \Delta p(r, \theta, \tau)\, d\theta = \frac{P(r,\tau)}{\rho} \delta(\theta), \tag{16}$$

$\delta(\theta)$ = Dirac delta function.

The velocity potential Φ in (15) is now written under the linearized lifting-line assumptions

$$\Phi(x^*, r^*, \theta_0^*; t) = -\frac{1}{4\pi U} \sum_k \int_{-\infty}^{x^*-x} d\nu \int_{r_f(\tau(\nu))}^{R} \frac{P(r,\tau)}{\rho} \frac{N_\nu}{R_\nu^3}\, dr. \tag{17}$$

Before calculating the induced velocities from Φ, all variable numbers will be non-dimensionalized and indicated by an overbar:

$$\bar{\Phi}(\bar{x}^*, \bar{r}^*, \theta_0^*; t) = -\tfrac{1}{2} \sum_k \int_{-\infty}^{\bar{x}^*} d\bar{\nu} \int_{\bar{r}_f(\tau(\bar{\nu}))}^{1} \bar{P}(r,\tau) \frac{\bar{N}_{\bar{\nu}}}{\bar{R}_{\bar{\nu}}^3}\, d\bar{r}, \tag{18}$$

where the normalization has been made as follows;

$$(\bar{x}^*, \bar{r}^*, \bar{x}, \bar{r}, \bar{\nu}) \equiv (x^*, r^*, x, r, \nu)/R,$$

$$\bar{\Phi} = \frac{\Phi}{RU}, \quad \bar{P} = \frac{P}{2\pi\rho U^2},$$

$$\bar{N}_{\bar{\nu}} = \frac{N_\nu}{R^2} = \bar{r}\,\bar{\nu} + \lambda \bar{r}^* \sin \bar{\Psi}_{\bar{\nu}} + (\bar{x}^* - \bar{\nu}) \frac{\bar{\lambda}_r \bar{r}}{\lambda} (\bar{r} - \bar{r}^* \cos \Psi_{\bar{\nu}}), \tag{19}$$

$$\bar{R}_{\bar{\nu}} = \mathscr{R}_\nu / R = [\bar{\nu}^2 + \bar{r}^2 + \bar{r}^{*2} - 2\bar{r}\,\bar{r}^* \cos \Psi_{\bar{\nu}}]^{\frac{1}{2}}, \tag{20}$$

$$\Psi_{\bar{\nu}} = -\omega t + \frac{\bar{x}^* - \bar{\nu}}{\lambda} - \theta_0^* + \sigma_k, \tag{21}$$

$$\bar{\lambda}_r = \lambda_r R.$$

Since a lifting-line approach is used, x and θ in (17) have been set to zero. Thus τ in (11) becomes

$$\tau = t - \frac{\bar{x}^* - \bar{\nu}}{\lambda \omega}. \tag{22}$$

The overbars used to identify the non-dimensional quantities will be dropped hereafter: all quantities from now on are non-dimensionalized. The induced velocities due to a series of the vortex sheets are then calculated:

$$\begin{aligned} u_{x^*}(x^*, r^*, \theta_0^*; t) &= \frac{\partial \Phi}{\partial x^*} \\ &= -\tfrac{1}{2} \sum_k \left\{ \int_{r_f(t)}^{1} \left[P(r, \tau(\nu)) \frac{N_\nu}{R_\nu^3} \right]\Big|_{\nu = x^*} + \int_{-\infty}^{x^*} P(r, \tau(\nu)) \frac{N_\nu}{R_\nu^3}\Big|_{r = r_f(t)} \right. \\ &\quad \left. \times \left(-\frac{\partial r_f}{\partial x^*} \right) d\nu + \int_d^1 dr \int_{-\infty}^{x^*} \frac{\partial}{\partial x^*} \left[P(r, \tau(\nu)) \frac{N_\nu}{R_\nu^3} \right] d\nu \right\}. \end{aligned} \tag{23}$$

It should be noted here that the order of integration between r and ν has been changed. This change has been made carefully, particularly for the integration limit in r; in order to cover the maximum blade-wetted length, the lower limit now should be d (the distance of the free surface measured from the centre of shaft, normalized by R). This does not mean that the induced velocities are independent of the time-varying blade-wetted length. Such effect is properly taken care of by the integration in the ν-direction; during the ν-integration, the arc length of integration

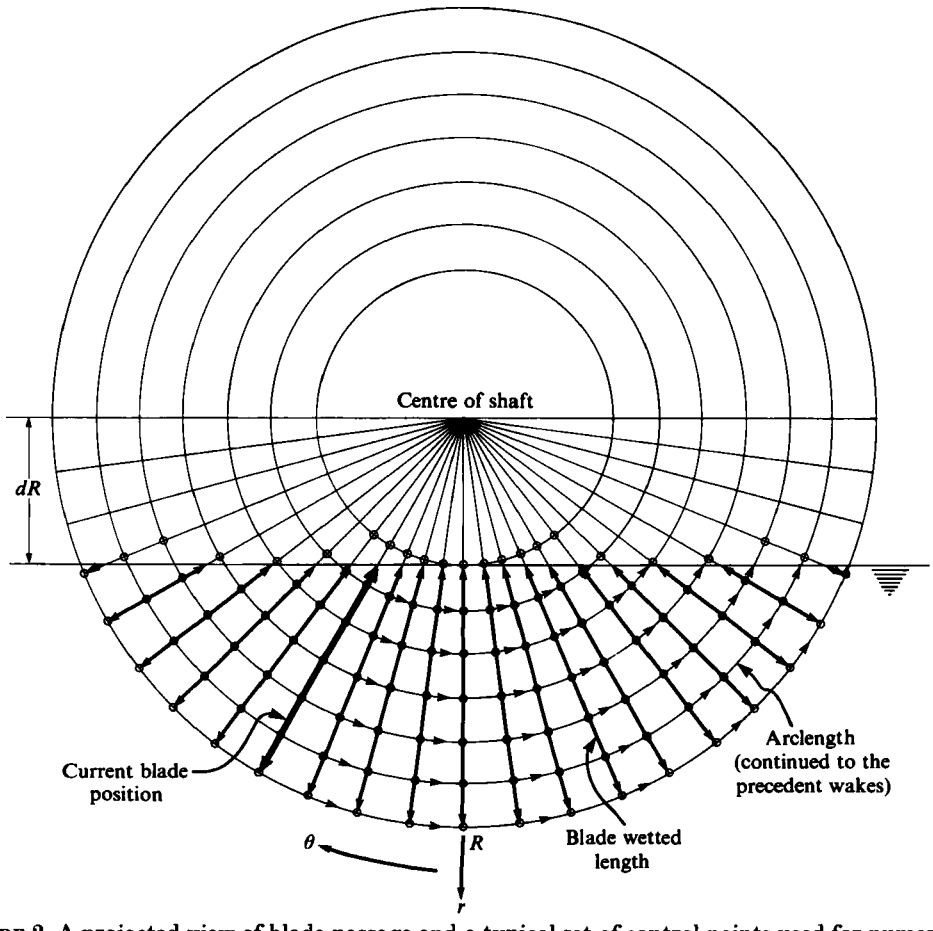

FIGURE 2. A projected view of blade passage and a typical set of control points used for numerical calculations when the control points ● and ○ denote those of finite loading and zero loading, respectively.

in the water layer at each fixed r varies since the blade-wetted length changes (see figure 2). Since $P(r, \tau(\nu))$ becomes zero at the free-surface, the second term disappears and thus:

$$u_{x^*} = -\tfrac{1}{2}\sum_k \left\{ \int_{r_1(t)}^{1} \left[P(r,\tau(\nu))\frac{N_\nu}{R_\nu^3} \right]\Big|_{\nu=x^*} + \int_d^1 \mathrm{d}r \int_{-\infty}^{x^*} \frac{\partial P(r,\tau(\nu))}{\partial x^*}\frac{N_\nu}{R_\nu^3}\,\mathrm{d}\nu \right.$$
$$\left. + \int_d^1 \mathrm{d}r \int_{-\infty}^{x^*} P(r,\tau(\nu))\frac{\partial}{\partial x^*}\left[\frac{N_\nu}{R_\nu^3}\right]\mathrm{d}\nu \right\}. \quad (24)$$

Furthermore, with the following identity,

$$\frac{\partial}{\partial x^*}\left[\frac{N_\nu}{R_\nu^3}\right] = \left(\frac{r}{R_\nu^3} - \frac{3\nu N_\nu}{R_\nu^5}\right) - \frac{\partial}{\partial \nu}\left[\frac{N_\nu}{R_\nu^3}\right],$$

(24) becomes

$$u_{x^*} = -\tfrac{1}{2}\sum_k \left\{ \int_{r_1(t)}^{1} P(r,\tau(\nu))\frac{N_\nu}{R_\nu^3}\Big|_{\nu=x^*}\mathrm{d}r + \int_d^1 \mathrm{d}r \int_{-\infty}^{x^*} \frac{\partial P(r,\tau(\nu))}{\partial x^*}\frac{N_\nu}{R_\nu^3}\,\mathrm{d}\nu \right.$$
$$\left. + \int_d^1 \mathrm{d}r \int_{-\infty}^{x^*} P(r,\tau(\nu))\left\{\frac{r}{R_\nu^3} - \frac{3\nu N_\nu}{R_\nu^5} - \frac{\partial}{\partial \nu}\left[\frac{N_\nu}{R_\nu^3}\right]\right\}\mathrm{d}\nu \right\}. \quad (25)$$

Integration by parts for the last integral I in (25) will yield

$$I \equiv \int_{\hat{d}}^{1} \mathrm{d}r \int_{-\infty}^{x^*} P(r,\tau(\nu))\left[\frac{r}{R_\nu^3}-\frac{3\nu N_\nu}{R_\nu^5}\right]\mathrm{d}\nu + \int_{\hat{d}}^{1} \mathrm{d}r\left\{\left[-P(r,\tau(\nu))\frac{N_\nu}{R_\nu^3}\right]\Big|_{-\infty} + \int_{-\infty}^{x^*} \frac{\partial P(r,\tau(\nu))}{\partial \nu}\frac{N_\nu}{R_\nu^3}\,\mathrm{d}\nu\right\}.$$

Since N_ν/R_ν^3 becomes zero as $\nu\to\infty$ and $\partial P/\partial\nu = -\partial P/\partial x^*$, by using (22), (25) can finally be written

$$u_{x^*} = -\tfrac{1}{2}\sum_k \int_{\hat{d}}^{1} \mathrm{d}r \int_{-\infty}^{x^*} P(r,\tau(\nu))\left(\frac{r}{R_\nu^3}-\frac{3\nu N_\nu}{R_\nu^5}\right)\mathrm{d}\nu. \tag{26}$$

This form is similar to the induced velocity in the x-direction obtained by Cox (1968) except that $P(r,\tau(\nu))$ here is a function of both r and time so that this term is now inside the integral for ν. It might not be immediately apparent that the loading term P in Cox's expression for the steady case could be moved into the ν-integral without the detailed derivation like the one made above.

The induced velocity in the tangential direction is obtained in a similar manner:

$$u_{\theta_0^*}(x^*, r^*, \theta_0^*; t) = \frac{1}{r^*}\frac{\partial \Phi}{\partial \theta_0^*} = -\tfrac{1}{2}\sum_k \left\{\int_{\hat{d}}^{1} \mathrm{d}r \int_{-\infty}^{x^*} \frac{1}{r^*}\frac{\partial}{\partial \theta_0^*}\left[P(r,\tau(\nu))\frac{N_\nu}{R_\nu^3}\right]\mathrm{d}\nu. \right. \tag{27}$$

Since $P(r,\tau(\nu))$ is independent of θ_0^*,

$$u_{\theta_0^*}(x^*, r^*, \theta_0^*; t) = -\tfrac{1}{2}\sum_k \left\{\int_{\hat{d}}^{1} \mathrm{d}r \int_{-\infty}^{x^*} P(r,\tau(\nu)) \times\left(\frac{-\lambda\cos\Psi_\nu + \frac{r}{\lambda}(\nu-x^*)\lambda_r \sin\Psi_\nu}{R_\nu^3} + \frac{3N_\nu r\sin\Psi_\nu}{R_\nu^5}\right)\mathrm{d}\nu\right\}. \tag{28}$$

A Hadamard numerical integral method (see the report of Mangler (1951) for a detailed treatment) for handling the singularities of fifth order in u_{x^*} and $u_{\theta_0^*}$ was used for (26) and (28). It was discovered, however, that there existed a numerical instability; the numerical results first converged as the mesh size of numerical control points decreased, but started diverging as the mesh size was further reduced. The Hadamard integral method which was successfully used for the airfoil integral, did not work properly due to the fifth-order singularities existing in the propeller integrals instead of the third-order singularities in the airfoil integrals. The present work was therefore devoted to fixing this numerically unstable problem by entirely changing the forms for u_{x^*} and $u_{\theta_0^*}$.

2.2. *Induction factors for unsteady wakes*

The philosophy adopted here for avoiding the numerical instability is similar to that of Moriya (1942), Lerbs (1952) and the work later elaborated on by Morgan & Wrench (1965). Since the propeller problem treated by these researchers was the steady flow one and thus had uniform wakes, they were able to introduce the idea of the induction factors. All integrals for obtaining the induction factors were reduced to those involving only the third-order singularities where the loading part was expressed in terms of the derivative with respect to r. By virtue of the steady flow assumption, they were finally converted into the series of Bessel functions. The real challenge for the present unsteady case will, therefore, be (i) to derive analytically the integral forms similar to those in the steady problem mentioned above, and then (ii) to assure

numerically the accuracy of the calculation of these integrals by having lower-order singularities.

First, the integral dummy variables ν in (26) and (28) are changed to new angular variables $\tilde{\theta}$ with the following relationship:

$$\tilde{\theta} = -\omega t - \frac{\nu - x^*}{\lambda} - \theta_0^*. \tag{29}$$

By rewriting the lifting-line induced velocities in the x- and θ-direction by a more conventional expression, i.e. w_a and w_t respectively, we can write

$$w_a \equiv u_{x^*}(x^*, r^*, \theta_0^*; t)$$
$$= -\tfrac{1}{2}\Sigma \int_d^1 \mathrm{d}r \int_0^\infty \lambda P(r, \tau(\tilde{\theta}))\left(\frac{r}{R_{\tilde{\theta}}^3} - \frac{3(-\lambda\tilde{\theta} + x^*)\, N_{\tilde{\theta}}}{R_{\tilde{\theta}}^5}\right)\mathrm{d}\tilde{\theta}, \tag{30}$$

$$w_t \equiv u_{\theta^*}(x^*, r^*, \theta_0^*; t)$$
$$= -\tfrac{1}{2}\Sigma \int_d^1 \mathrm{d}r \int_0^\infty \lambda P(r, \tau(\tilde{\theta}))\left(\frac{-\lambda \cos \Psi_{\tilde{\theta}} - \lambda_r r\tilde{\theta} \sin \Psi_{\tilde{\theta}}}{R_{\tilde{\theta}}^3} + \frac{3N_{\tilde{\theta}} r \sin \Psi_{\tilde{\theta}}}{R_{\tilde{\theta}}^5}\right)\mathrm{d}\tilde{\theta}, \tag{31}$$

where

$$R_{\tilde{\theta}} = [(-\lambda\tilde{\theta} + x^*)^2 + r^2 + r^{*2} - 2rr^* \cos \Psi_{\tilde{\theta}}]^{\frac{1}{2}},$$

$$N_{\tilde{\theta}} = r(-\lambda\tilde{\theta} + x^*) + \lambda r^* \sin \Psi_{\tilde{\theta}} + \lambda_r r\tilde{\theta}(r - r^* \cos \Psi_{\tilde{\theta}}),$$

$$\Psi_{\tilde{\theta}} = \tilde{\theta} + \theta_0^* + \sigma_k,$$

$$\theta_0^* = -\omega t - \theta_0^* \text{ (this value will be zero for the induced velocity calculation on the lifting line itself since } \theta_0^* = -\omega t),$$

$$\lambda = U(r)/\omega R,$$

$$\lambda_r = (\mathrm{d}\lambda/\mathrm{d}r)\, R \text{ (since this is a non-dimensional expression).}$$

Since P is a function of both r and $\tilde{\theta}$, the following identities have been derived successfully after lengthy algebraic computations:

$$\frac{r}{R_{\tilde{\theta}}^3} - \frac{3(-\lambda\tilde{\theta} + x^*)\, N_{\tilde{\theta}}}{R_{\tilde{\theta}}^5} = -\frac{\partial}{\partial r}\left[\frac{r(r - r^* \cos \Psi_{\tilde{\theta}})}{R_{\tilde{\theta}}^3}\right] - \frac{\partial}{\partial\tilde{\theta}}\left[\frac{r^* \sin \Psi_{\tilde{\theta}}}{R_{\tilde{\theta}}^3}\right], \tag{32}$$

$$\frac{-\lambda \cos \Psi_{\tilde{\theta}} - \lambda_r r\tilde{\theta} \sin \Psi_{\tilde{\theta}}}{R_{\tilde{\theta}}^3} + \frac{3N_{\tilde{\theta}} r \sin \Psi_{\tilde{\theta}}}{R_{\tilde{\theta}}^5}$$
$$= -\frac{\partial}{\partial r}\left[\frac{\lambda(r^* - r \cos \Psi_{\tilde{\theta}}) + (-\lambda\tilde{\theta} + x^*)\, r \sin \Psi_{\tilde{\theta}}}{R_{\tilde{\theta}}^3}\right]$$
$$+ \frac{\partial}{\partial\tilde{\theta}}\left[\frac{-(-\lambda\tilde{\theta} + x^*) \cos \Psi_{\tilde{\theta}} + \lambda_r \tilde{\theta}(r^* - r \cos \Psi_{\tilde{\theta}})}{R_{\tilde{\theta}}^3}\right]. \tag{33}$$

By using these identities, the kernel function of the integrals for w_a and w_t in (30) and (31) will be converted into the radial and tangential derivative forms with only the third-order singularities. Performing integration by parts in terms of r and $\tilde{\theta}$, we obtain

$$w_a(x^*, r^*, \theta_0^*; t) = -\tfrac{1}{2}\sum_k \int_0^\infty \mathrm{d}\tilde{\theta} \int_{r_t(\tau(\tilde{\theta}))}^1 \left\{\frac{\partial}{\partial r}[\lambda P(r, \tau(\tilde{\theta}))]\right\} \frac{r(r - r^* \cos \Psi_{\tilde{\theta}})}{R_{\tilde{\theta}}^3}\, \mathrm{d}r$$
$$-\tfrac{1}{2}\Sigma \int_d^1 \mathrm{d}r \int_0^\infty \lambda \frac{\partial P(r, \tau(\tilde{\theta}))}{\partial\tilde{\theta}} \frac{r^* \sin \Psi_{\tilde{\theta}}}{R_{\tilde{\theta}}^3}\, \mathrm{d}\tilde{\theta} \tag{34}$$

and

$$w_t(x^*, r^*, \theta_0^*; t)$$

$$= -\tfrac{1}{2}\sum_k \int_0^\infty d\tilde{\theta} \int_{r_t(\tau(\tilde{\theta}))}^1 \left\{\frac{\partial}{\partial r}[\lambda P(r, \tau(\tilde{\theta}))]\right\} \frac{\lambda(r^* - r\cos\Psi_{\tilde{\theta}}) + (-\lambda\tilde{\theta} + x^*) r \sin\Psi_{\tilde{\theta}}}{R_{\tilde{\theta}}^3} dr$$

$$+ \tfrac{1}{2}\sum_k \int_d^1 dr \int_0^\infty \lambda \frac{\partial P(r, \tau(\tilde{\theta}))}{\partial\tilde{\theta}} \frac{-(-\lambda\tilde{\theta} + x^*)\cos\Psi_{\tilde{\theta}} + \lambda_r \tilde{\theta}(r^* - r\cos\Psi_{\tilde{\theta}})}{R_{\tilde{\theta}}^3} d\tilde{\theta}. \quad (35)$$

It is seen clearly from these results that the induced velocities obtained here consist of two parts, i.e. the steady part relating to $\partial(\lambda P)/\partial r$ and the unsteady part relating to $\partial P/\partial\tilde{\theta}$. For the case of the steady propeller flow problem, $\partial P/\partial\theta$ becomes zero and $\partial P/\partial r$ becomes independent of $\tilde{\theta}$. w_a and w_t in (34) and (35) will be reduced to a form identical with those of the steady flow case in Cox (1968). It is considered that the present results will be extremely useful, not only to the current partially submerged propeller problems, but also in analysing any general unsteady propeller flows.

w_a and w_t in (34) and (35) can be further modified for securing numerical stability:

$$w_a = -\frac{1}{2}\int_d^1 \frac{I_{ar}(r, r^*)}{r - r^*} dr - \frac{1}{2}\int_d^1 \frac{I_{a\tilde{\theta}}(r, r^*)}{r - r^*} dr, \quad (36)$$

$$w_t = -\frac{1}{2}\int_d^1 \frac{I_{tr}(r, r^*)}{r - r^*} dr + \frac{1}{2}\int_d^1 \frac{I_{t\tilde{\theta}}(r, r^*)}{r - r^*} dr, \quad (37)$$

where

$$I_{ar}(r, r^*) = \sum_k \int_0^\infty \left\{\frac{\partial}{\partial r}[\lambda P(r, \tau(\tilde{\theta}))]\right\} \frac{(r - r^*) r(r - r^*\cos\Psi_{\tilde{\theta}})}{R_{\tilde{\theta}}^3} d\tilde{\theta}, \quad (38)$$

$$I_{a\tilde{\theta}}(r, r^*) = \sum_k \int_0^\infty \lambda \frac{\partial P(r, \tau(\tilde{\theta}))}{r\,\partial\tilde{\theta}} \frac{r(r - r^*) r^* \sin\Psi_{\tilde{\theta}}}{R_{\tilde{\theta}}^3} d\tilde{\theta}, \quad (39)$$

$$I_{tr}(r, r^*) = \sum_k \int_0^\infty \left\{\frac{\partial}{\partial r}[\lambda P(r, \tau(\tilde{\theta}))]\right\} \times \frac{(r - r^*)\{\lambda(r^* - r\cos\Psi_{\tilde{\theta}}) + (-\lambda\tilde{\theta} + x^*) r \sin\Psi_{\tilde{\theta}}\}}{R_{\tilde{\theta}}^3} d\tilde{\theta}, \quad (40)$$

$$I_{t\tilde{\theta}}(r, r^*) = \sum_k \int_0^\infty \lambda \frac{\partial P(r, \tau(\tilde{\theta}))}{r\,\partial\tilde{\theta}} \times \frac{r(r - r^*)\{-(-\lambda\tilde{\theta} + x^*)\cos\Psi_{\tilde{\theta}} + \lambda_r \tilde{\theta}(r^* - r\cos\Psi_{\tilde{\theta}})\}}{R_{\tilde{\theta}}^3} d\tilde{\theta}, \quad (41)$$

and the integration order between r and $\tilde{\theta}$ has been changed with the same justification as for (23). I_{ar}, $I_{a\tilde{\theta}}$, I_{tr}, $I_{t\tilde{\theta}}$ in (38)–(41) are similar to the induction factors introduced by Lerbs (1952), who developed the steady-state propeller lifting-line theory. In the steady-state problem $(\partial/\partial r)[\lambda P(r, \tau(\tilde{\theta}))]$ is independent of $\tilde{\theta}$, so that this term can be taken out of the $\tilde{\theta}$-integrals. Without the terms of $(\partial/\partial r)[\lambda P(r, \tau(\tilde{\theta}))]$, I_{ar} and I_{tr} should be identical with the induction factors of Lerbs, who calculated them in a totally different way, as mentioned before. In order to test the accuracy of the numerical integral method to be employed for the present analysis, I_{ar} and I_{tr} in (38) and (40) were numerically calculated with $\partial(\lambda P)/\partial r = 1$, $x_0^* = 0$ and $\theta_0^* = -\omega t$ for various r/r^* ratios and β_{i0} (flow pitch angles) by applying Simpson's rule. It was found that for large β_{i0} such as 60° and r/r^* ratios larger than 0.6, I_{ar} and I_{tr} agreed with those of Lerbs to an accuracy within 0.1 % for ten turns of wakes, whereas, for smaller β_{i0} such as 15° and r/r^* less than 0.6, the errors were about 3 %.

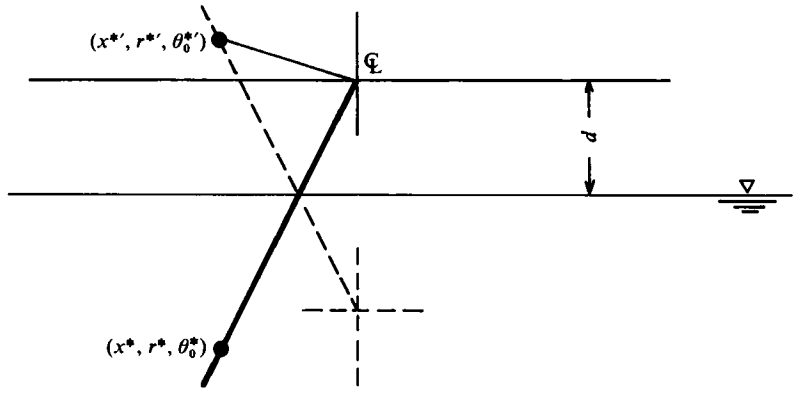

FIGURE 3. Mirror image point used for the second method of calculating the induced velocity effect due to the image wakes.

However, the accuracy greatly improved if twenty turns of wakes were taken for the numerical calculations, with the accuracy less than 1 % for all combinations of β_{i0} and r/r^*. Furthermore, since the errors were observed at only small r/r^*, they would play a negligibly small role in the overall integral with respect to r for the final values of w_a and w_t (a sample case showed an error less than 0.1 %). Also, I_{ar} and I_{tr} values calculated with the present method showed smooth transition near $r/r^* = 1$, taken to be unity. Finally, reducing the integral intervals in both $\tilde{\theta}$ and r made the calculated values of the integrals converge to single numbers.

It has now been determined that by applying the integral method mentioned above to I_{ar}, $I_{a\tilde{\theta}}$, I_{tr} and $I_{t\tilde{\theta}}$, with P varying as a function of $\tilde{\theta}$ owing to the flow unsteadiness, we can obtain accurate and numerically stable induced velocities for the present partially submerged propeller problem.

The method for obtaining the image-induced velocities is rather simple; instead of constructing the image wake system in the air domain, we will first obtain the mirror image for the point of interest on the lifting-line and then obtain the induced velocities due to the real wake systems. In this flow configuration, the relative geometry between the point of interest and wake system is identical to the one considered above except that the wake helical windings are in the opposite direction. This means that the induced velocity in the x-direction will be added to the real part, whereas that in the tangential direction will have to be subtracted from the counterpart.

The only work needed to implement the above method is to obtain new coordinates for the point of the lifting-line in the water, i.e. (x^*, r^*, θ_0^*). Defining the image point by $(x^{*\prime}, r^{*\prime}, \theta_0^{*\prime})$, one will readily find the following relationships (see figure 3):

$$\left.\begin{aligned} x^{*\prime} &= x^* = 0, \\ r^{*\prime} \cos\theta_0^{*\prime} &= r^* \cos\theta_0^*, \\ r^* \sin\theta_0^* + r^{*\prime} \sin\theta_0^{*\prime} &= 2d. \end{aligned}\right\} \tag{42}$$

It is straightforward to obtain $(x^{*\prime}, r^{*\prime}, \theta_0^{*\prime})$ from (42) once (x^*, r^*, θ_0^*) are given. These new coordinate points will be substituted into (36) and (37) to obtain the induced velocities ω_a and ω_t due to the image wakes:

$$\omega_a = w_a(0, r^{*\prime}, \theta_0^{*\prime}(t); t) \quad \text{in (36)}, \tag{43}$$

$$\omega_t = w_t(0, r^{*\prime}, \theta_0^{*\prime}(t); t) \quad \text{in (37)}. \tag{44}$$

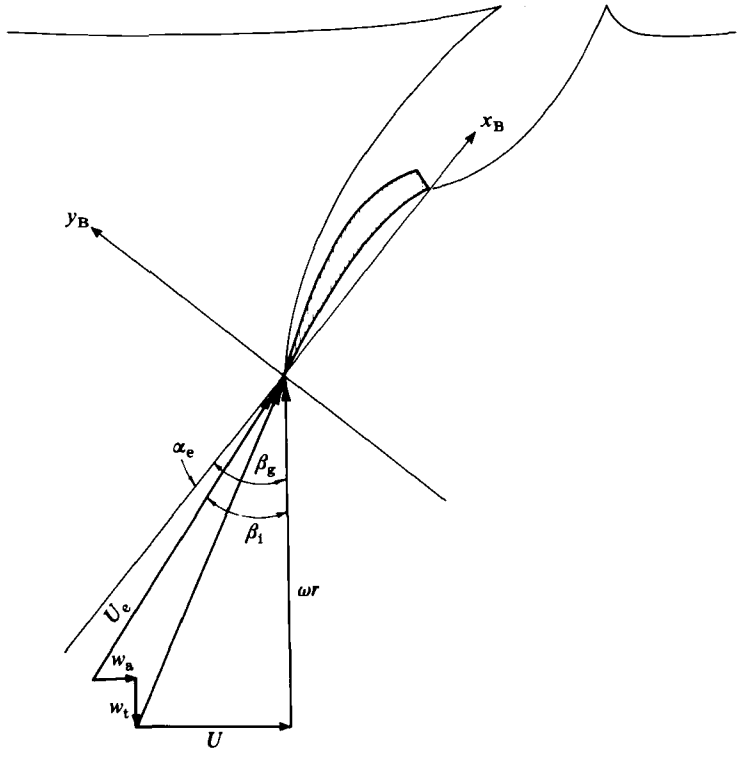

FIGURE 4. Local flow configuration in the two-dimensional plane.

The total induced velocities are finally obtained as follows:

$$\Sigma w_a = w_a(0, r^*, -\omega t; t) + \omega_a(0, r^{*\prime}, \theta_0^{*\prime}(t); t), \tag{45}$$

$$\Sigma w_t = w_t(0, r^*, -\omega t; t) + \omega_t(0, r^{*\prime}, \theta_0^{*\prime}(t); t). \tag{46}$$

3. Solution method

The off-design propeller problem to be solved here is to satisfy the velocity vector relationship shown in figure 4, i.e.

$$\tan\beta_i = \frac{U + \Sigma w_a}{\omega r - \Sigma w_t} \tag{47}$$

$$\tan\{\beta_g(r^*) - \alpha_e(r^*)\}\left[\frac{\pi r^*}{J} - \Sigma w_a(P(r^*, \alpha_e(r^*), t))\right] - [1 + \Sigma w_t(P(r^*, \alpha_e(r^*), t))] = 0 \quad \text{for all } r^*, \tag{48}$$

where β_g is a propeller geometric parameter, see figure 4. In (48), the P-function should be determined as functions of r^* and time (or the relative position of the blade in reference to the free surface).

The relationship between the lifting forces and the P-function will be given as follows:

$$\lambda P = \frac{1}{4\pi}\frac{U_e}{U} C_L\left(\frac{c}{R}\right), \tag{49}$$

where $c \equiv$ chord,

$U_e \equiv$ effective relative velocity,

$= [(U+w_a)^2+(\omega r+w_t)^2]^{\frac{1}{2}}$,

$C_L \equiv$ lift coefficient,

$U \equiv V_a$ if no wake reduction factor is considered.

In order to account for the induced-flow effects on the location of the vortex sheets, use of $\lambda_i(r)$ instead of $\lambda(r)$ is recommended, where

$$\lambda_i(r) = x \tan\beta_i = \frac{U+\Sigma\, w_a(r)}{\omega r-\Sigma\, w_t(r)}\frac{r}{R}. \tag{50}$$

Unlike the Prandtl type of steady-state three-dimensional wing problem, the P-function cannot be expressed conveniently in terms of Fourier series for two reasons. First, P is an intermittent function of time, increasing from zero to the maximum value, decreasing back to zero when the blade is out of water and staying zero until the next entry of the blade into water. Secondly the span length of a blade continuously changes as it moves and the P-function does not have similarity even for the normalized span scale.

We propose a method for solution which will employ a numerical iterative method as in Furuya (1980). First, we use the geometric incidence angle at each blade spanwise position to calculate the lifting force as a function of blade location or time. D. P. Wang's (1979) blade entry and exit theory will be used to evaluate this loading function P through (48) by assuming $\Sigma\, w_a = \Sigma\, w_t = 0$. Once the initial distribution of P is given as functions of r^* and t, the induced flow velocities $\Sigma\, w_a$ and $\Sigma\, w_t$ will be calculated from the formula obtained in the previous section. These induced velocities now change the local effective flow incidence angles α_e. With a new set of α_e, a new loading function P is calculated again with the two-dimensional water entry–exit method. This iterative procedure will be repeated until a convergent solution is obtained.

4. Calculations of two-dimensional sectional loadings with D. P. Wang's program

In order to determine the strength of circulation at various blade radial stations in the propeller lifting-line theory, the two-dimensional lifting force must be described as functions of blade geometry, angle of incidence, submergence depth and angle of entry or exit. D. P. Wang (1979) recently developed the theory for solving the problem of oblique water entry and exit for a fully ventilated foil. The theory employed a linearized initial-value problem approach for the mixed-typed boundary condition. However, the computer program developed there is only applicable to foils having straight line and circular arc camber profiles. In practice, ventilating propellers under the partially submerged condition are usually designed to have a somewhat different type of foil profile shape. One of the most frequently used blade profiles for this type of propeller is the two-term camber of Tulin–Bukart (1955), which is expressed in the following equation:

$$y_B = \tfrac{1}{2}A(x_B+\tfrac{8}{3}x_B^{\frac{3}{2}}-4x_B^2)+Bx_B, \tag{51}$$

	Model 3768		Model 4002	
r/R	A	B	A	B
0.2	0.01718	0.00286	0	0
0.3	0.08446	0.01408	0.05833	0.00972
0.4	0.11974	0.01996	0.08333	0.01389
0.5	0.13748	0.02291	0.09552	0.01592
0.6	0.14516	0.02419	0.09583	0.01597
0.7	0.14514	0.02419	0.08729	0.01455
0.8	0.13606	0.02268	0.07982	0.01330
0.9	0.12734	0.02122	0.08855	0.01476

TABLE 1. Two-term camber profiles for NSRDC propeller models 3768 and 4002 (see Hadler & Hecker (1968)) defined by $y_B = \frac{1}{4}A(x_B + \frac{8}{3}x_B^{\frac{1}{2}} - 4x_B^2) + Bx_B$, equation (51).

where the first group of terms in the brackets is the two-term camber part and Bx is merely a rotation of the (x, y)-coordinates. It is readily understood that the terms related to x and x^2 represent the straight line and circular arc profiles, respectively, whereas a term proportional to $x^{\frac{3}{2}}$ is the specific term in the two-term camber profile. Incidentally, the partially submerged propellers, Models 3767 and 4002, tested by Hadler & Hecker (1968) had the two-term camber expressed in (51). Table 1 presents the values of coefficients A and B at various radial stations. More generally, supercavitating or fully ventilated blade profiles can be written

$$y_B = \sum_{n=0}^{m} a_n x_B^{\frac{1}{2}n}. \tag{52}$$

In order to handle these general blade profile cases the Wang's computer code needed modification involving detailed understanding of the various variable transformation and singularity removal techniques used in the program. After this modification was made, the program has become much easier for users to incorporate any type of blade profile shape such as expressed in (51) or (52); the only change of the computer code to be made for different types of profile now is that of a subroutine specifying the profile shape.

With this modified computer code we made computations for lift and drag forces for the Tulin–Bukart two-term camber at various water depths and angles of blade entry and exit, the results being shown in figures 5–8. Use will be made of these graphs as follows. Assuming that the two-term camber is given by (51) with h/π and λ, the force coefficients for the two-term camber and straight line can be read from each graph. The total C_L and C_D will then be calculated:

$$\begin{pmatrix} C_L \\ C_D \end{pmatrix} = \frac{A}{A_d}\begin{pmatrix} C_{L(2-T)} \\ C_{D(2-T)} \end{pmatrix} - 10(B - \alpha_e)\begin{pmatrix} C_{L(\text{Flat})} \\ C_{D(\text{Flat})} \end{pmatrix}, \tag{53}$$

where $A_d = 0.10186$, which corresponds to $C_{Ld} = 0.2$, and α_e denotes the flow incidence angle. This calculation should be made for all h/π and λ since the specified h/π and λ for which C_L and C_D are to be calculated are usually different from those for which the present computation was made. Then an interpolation method is necessary in h/π and λ planes to finally determine C_L and C_D for the specified values of h/π and λ. The computer code developed for the propeller calculation uses one such interpolation scheme. Incidentally, the accuracy of the modified Wang computer code

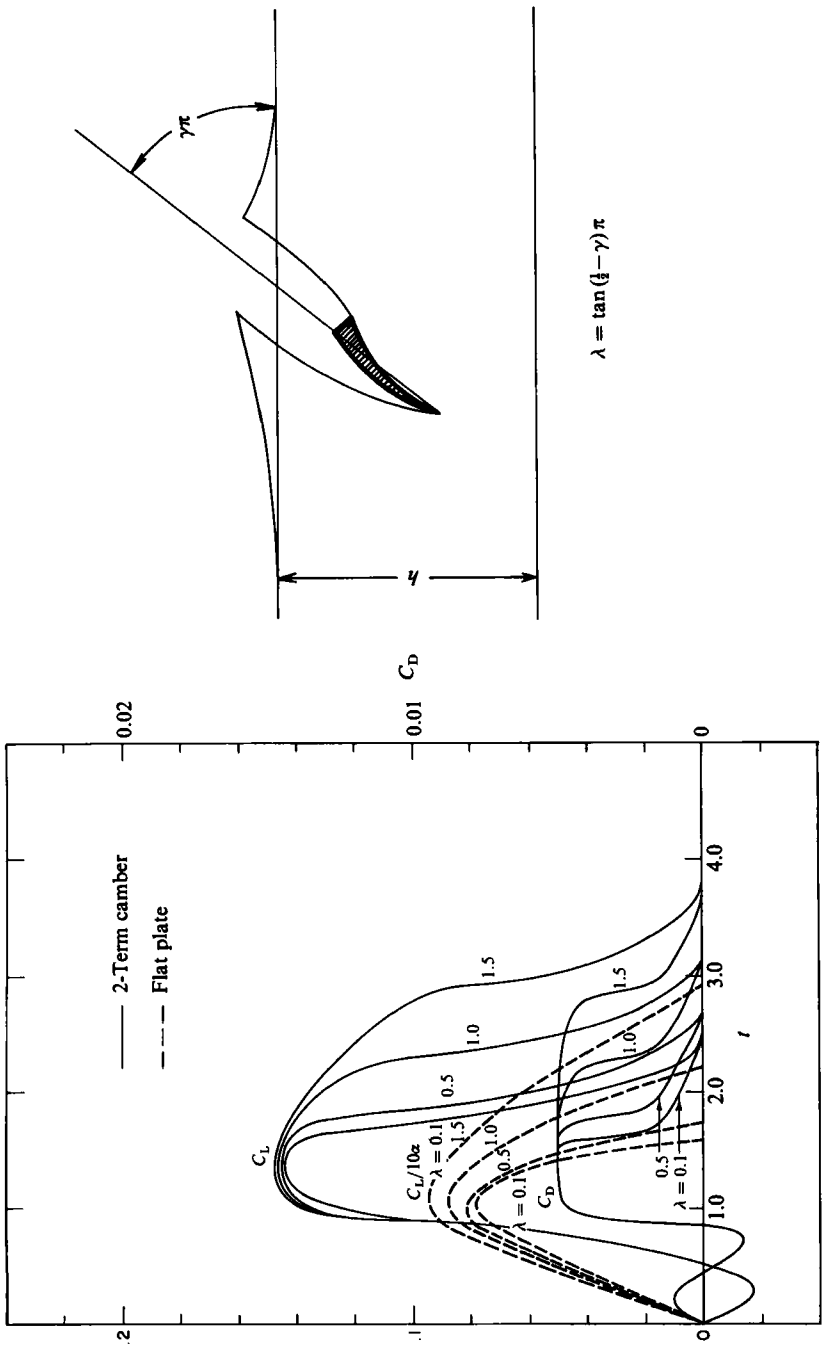

FIGURE 5. Two-dimensional lift and drag coefficients for Tulin–Bukart two-term camber and flat plate calculated with Wang's theory (1979) where $A_d = 0.10186$ (i.e. $C_{LD} = 0.20$) has been used in (51) and $h/\pi = 0.5$.

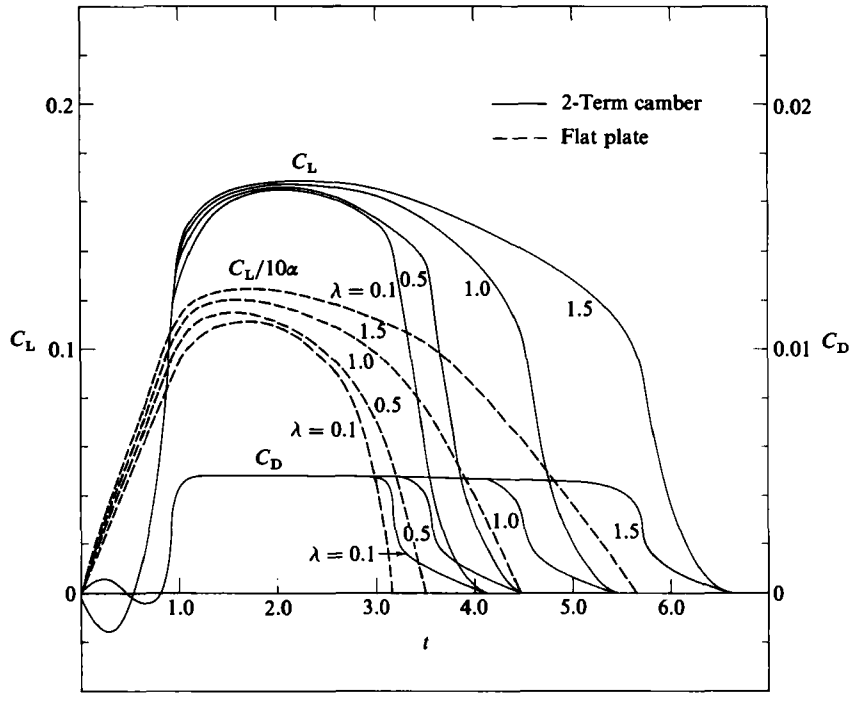

FIGURE 6. As figure 4 except that $h/\pi = 1.0$.

was checked by increasing h/π values to 5, 10, etc. for the two-term camber, and it was observed that calculated C_L values asymptotically approached 0.2. Since A_d used here corresponds to the lift coefficient when $C_{Ld} = 0.2$, it was considered that the accuracy of the computer code, as well as the theory, has been proved.

One of the most interesting features regarding the two-term camber used for the partially submerged propeller appears in the results of the calculations for the present two-dimensional sectional characteristics. For a short time period immediately after a blade leading-edge entry into the water, the lifting forces for the two-term camber show negative values. As the blade proceeds and has a larger submergence, these negative values turn around and rapidly change to positive values. This means that the blade tip material experiences the oscillatory force from a negative to a positive value at each cycle of rotation. The reason for this phenomenon can readily be understood if one closely investigates the profile shape of the two-term camber, particularly near the leading edge where negative slope exists (see figure 9). When only the blade tip is plunged into water, the lifting force is naturally negative. However, as a larger portion of the blade is submerged into the water, the positive camber starts taking effect and thus the direction of force changes.

Also, these lift and drag forces during such a critical period were calculated on the assumption that the face portion of the blade is wetted and the back portion has ventilation. This assumption may be erroneous; the flow configuration to be used for such a case is that the face part must have ventilation whereas the back part must be fully wetted. As the blade proceeds, the water starts filling in the face part, possibly trapping the air near the leading edge while the back part cannot sustain the negative pressure so that cavitation and/or ventilation may suddenly take place. Therefore

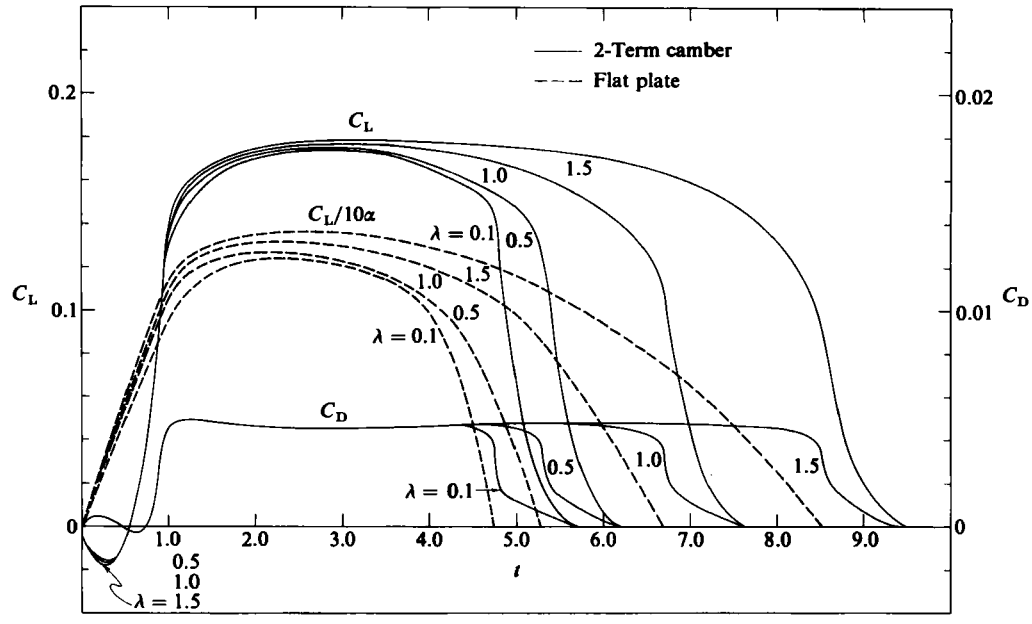

FIGURE 7. As figure 4 except that $h/\pi = 1.5$.

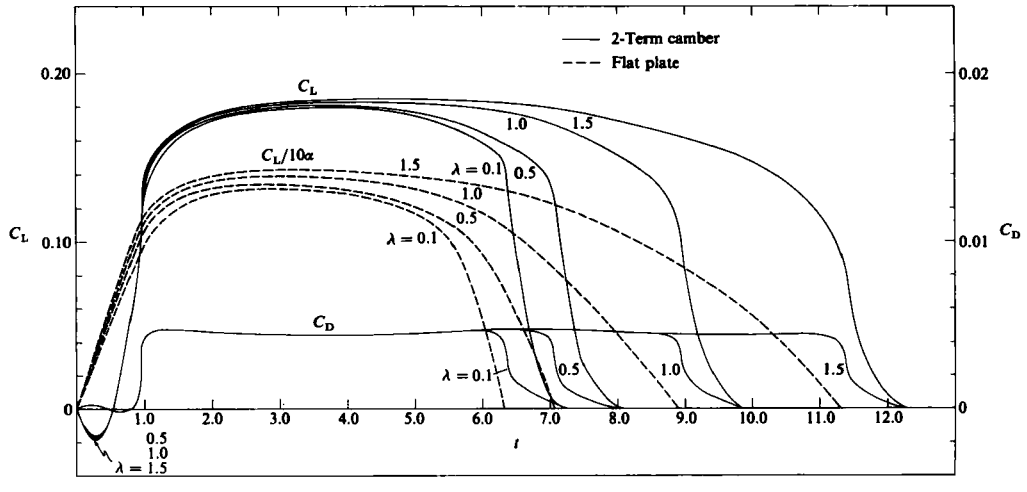

FIGURE 8. As figure 4 except that $h/\pi = 2.0$.

the change of forces near the leading edge may be even more drastic than is shown in figures 5–8; it could even be of impulse type.

In any case, this type of repeated oscillatory force will easily lead to material failure due to fatigue phenomena. According to private communications with D. P. Wang and from other documents, the partially submerged propeller can survive only for a few hours of operation, ending with material breakdown. As a matter of fact, most of the partially submerged propellers designed to date employ the two-term or similar camber profiles (see table 1). The findings mentioned here suggest that the use of the two-term or higher-order cambers, known to be superior in the area of fully submerged

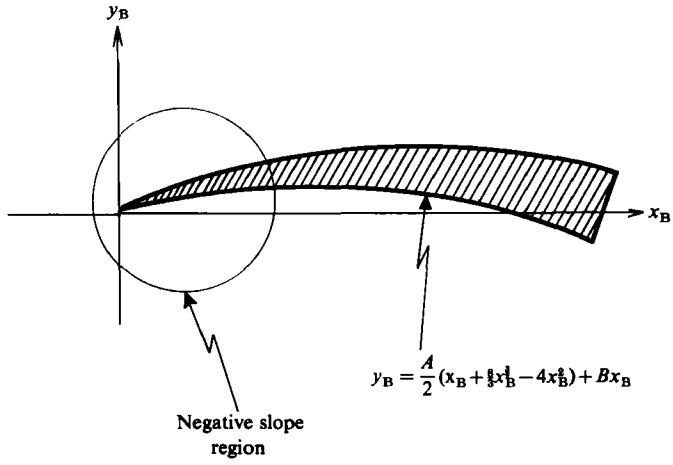

FIGURE 9. Schematic diagram for Tulin–Bukart two-term camber.

supercavitating propellers, are not necessarily suitable for the environment encountered by the partially submerged propeller. Since material failure is the most critical problem in this type of propeller design, the selection of the propeller blade profile needs specific consideration for material integrity as well as for avoidance of oscillatory forces at the time of entry. One of the possible candidates for the leading-edge profile used for the partially submerged propeller may be that of smooth straight line, wedge type or even finite thickness with a rounded leading edge followed by an appropriate camber profile.

5. Thrust and power coefficients

The time-averaged thrust and power coefficients $\bar{C}_T$ and $\bar{C}_P$ can be calculated as follows. The thrust and power forces for the kth blade at an instantaneous time t or equivalently at a rotational angle θ (see figure 2) are given as:

$$T(\theta+\sigma_k) = \int_{dR}^{R} \{C_L \tfrac{1}{2}\rho U_e^2 C \cos\beta_i - (D+D_f)\sin\beta_i\}\,dr, \tag{54}$$

$$P(\theta+\sigma_k) = \int_{dR}^{R} \omega r\{C_L \tfrac{1}{2}\rho U_e^2 C \sin\beta_i + (D+D_f)\cos\beta_i\}\,dr, \tag{55}$$

where

D = form drag on the blade, $D(r,\theta)$,

D_f = friction drag, $D_f(r,\theta)$,

$U_e = [(\omega r - \Sigma\, w_t)^2 + (U + \Sigma\, w_a)^2]^{\frac{1}{2}}$ (see figure 4),

$\beta_i = \tan^{-1}\dfrac{U+\Sigma\, w_a}{\omega r - \Sigma\, w_t}$ (see figure 4).

First T and P are normalized:

$$\bar{C}_T(\theta+\sigma_k) = \frac{T(\theta+\sigma_k)}{\frac{1}{2}\rho U^2 \pi R^2}$$

$$= 4\int_d^1 \left\{\frac{U_e}{U}\lambda P\cos\beta_i - \frac{1}{4\pi}(C_D + C_{Df})\,\bar{c}\left(\frac{U_e}{U}\right)^2 \sin\beta_i\right\} d\bar{r}.$$

$$\bar{C}_{\mathrm{P}}(\theta+\sigma_k) = \frac{P(\theta+\sigma_k)}{\frac{1}{2}\rho U^3 \pi R^2},$$

$$= \frac{4}{\pi}\int_{\bar{d}}^{1} \bar{r}\left\{\frac{U_{\mathrm{e}}}{U}\lambda P \sin\beta_{\mathrm{i}} + \frac{1}{4\pi}(C_{\mathrm{D}}+C_{\mathrm{Df}})\,\bar{c}\left(\frac{U_{\mathrm{e}}}{U}\right)^2 \cos\beta_{\mathrm{i}}\right\} \mathrm{d}\bar{r},$$

where

$$\lambda P = \frac{1}{4\pi}\frac{U_{\mathrm{e}}}{U}\bar{c}\,C_{\mathrm{L}},$$

$$C_{\mathrm{L}} = \frac{L}{\frac{1}{2}\rho U_{\mathrm{e}}^2 \bar{c}},$$

$$C_{\mathrm{D}} = \frac{D}{\frac{1}{2}\rho U_{\mathrm{e}}^2 \bar{c}},$$

$$C_{\mathrm{Df}} = \frac{D_{\mathrm{f}}}{\frac{1}{2}\rho U_{\mathrm{e}}^2 \bar{c}},$$

$\bar{c}$ = normalized chord ($= c/R$).

In order to obtain the averaged thrust and power coefficients $\bar{C}_{\mathrm{T}}$ and $\bar{C}_{\mathrm{P}}$, T_k and P_k must be integrated over one rotation of propeller and then be divided by 2π:

$$\bar{C}_{\mathrm{T}} = \frac{1}{2\pi}\int_0^{2\pi}\left\{\sum_{k=1}^{K}\bar{C}_{\mathrm{T}}(\theta+\sigma_k)\right\}\mathrm{d}\theta, \tag{56}$$

$$\bar{C}_{\mathrm{P}} = \frac{1}{2\pi}\int_0^{2\pi}\left\{\sum_{k=1}^{K}\bar{C}_{\mathrm{P}}(\theta+\sigma_k)\right\}\mathrm{d}\theta. \tag{57}$$

The conversion of $\bar{C}_{\mathrm{T}}$ and $\bar{C}_{\mathrm{P}}$ into more conventional thrust and torque coefficients $\bar{K}_{\mathrm{T}}$ and $\bar{K}_{\mathrm{Q}}$ is a simple matter, i.e.

$$\bar{K}_{\mathrm{T}} = \frac{\pi J^2}{8}\bar{C}_{\mathrm{T}}, \tag{58}$$

$$\bar{K}_{\mathrm{Q}} = \frac{J^3}{16}\bar{C}_{\mathrm{P}}, \tag{59}$$

where the definition of $\overline{K}_{\mathrm{T}}$ and $\overline{K}_{\mathrm{Q}}$ is given by

$$\overline{K}_{\mathrm{T}}(\theta+\sigma_k) = \frac{T(\theta+\sigma_k)}{16\rho n^2 R^4}, \tag{60}$$

$$\overline{K}_{\mathrm{Q}} = \frac{P(\theta+\sigma_k)}{32\rho n^2 R^5}. \tag{61}$$

The averaged efficiency of the propeller is thus

$$\bar{\eta} = \frac{\bar{C}_{\mathrm{T}}}{\bar{C}_{\mathrm{P}}} = \frac{\bar{K}_{\mathrm{T}}}{\bar{K}_{\mathrm{Q}}}\frac{J}{2\pi}. \tag{62}$$

6. Results

The computer program was developed on the basis of the new theory and was applied for calculating the off-design performance of two different types of partially submerged propellers: NSRDC Propeller Model 3768 and 4002. The geometric

	Model 3768	Model 4002
Diameter	10 in.	12 in.
Number of blades	3	2
Camber	2-term camber (see table 1)	2-term camber (see table 1)
P/D at $x = 0.7$	1.180	1.319

TABLE 2. Propeller characteristics of NSRDC propeller models 3768 and 4002

	Model 3768		Model 4002	
Radial station/R	Chord/R	Geometric blade angle β_g	Chord/R	Geometric blade angle β_g
0.2	0.7640	61.966°	0.6876	64.118°
0.3	0.7640	51.385°	0.6876	54.049°
0.4	0.7640	43.199°	0.6876	46.033°
0.5	0.7620	36.914°	0.6858	39.767°
0.6	0.7460	32.047°	0.6714	34.850°
0.7	0.7020	28.217°	0.6318	30.949°
0.8	0.6120	25.150°	0.5508	27.816°
0.9	0.4600	22.653°	0.4140	25.250°

TABLE 3. Detailed blade characteristics of propeller models 3768 and 4002

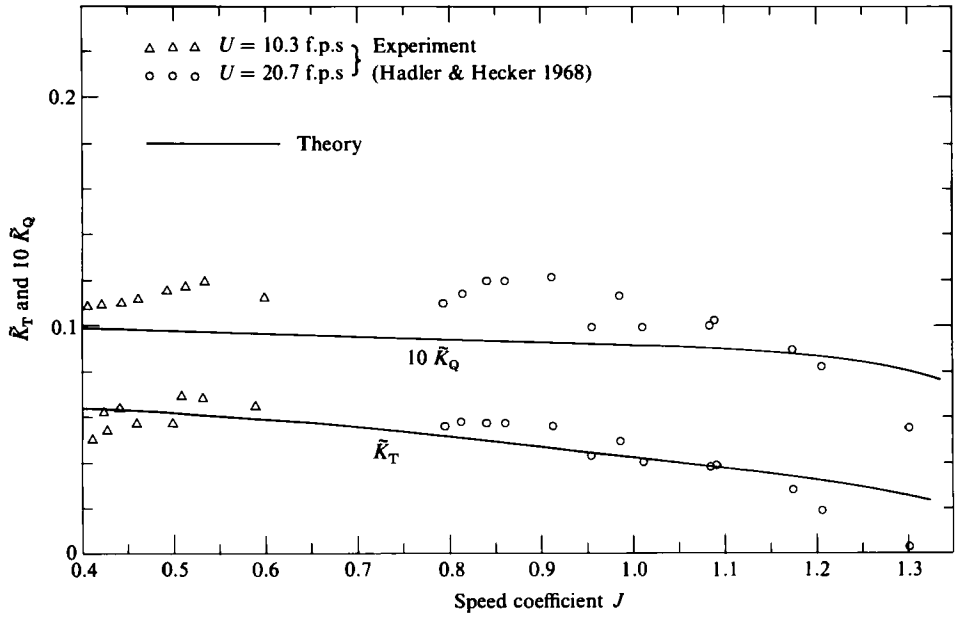

FIGURE 10. Comparison between the present theory and experimental data of Hadler & Hecker (1968) for $\tilde{K}_T$ and $\tilde{K}_Q$ of propeller model 3768 at submergence 40%.

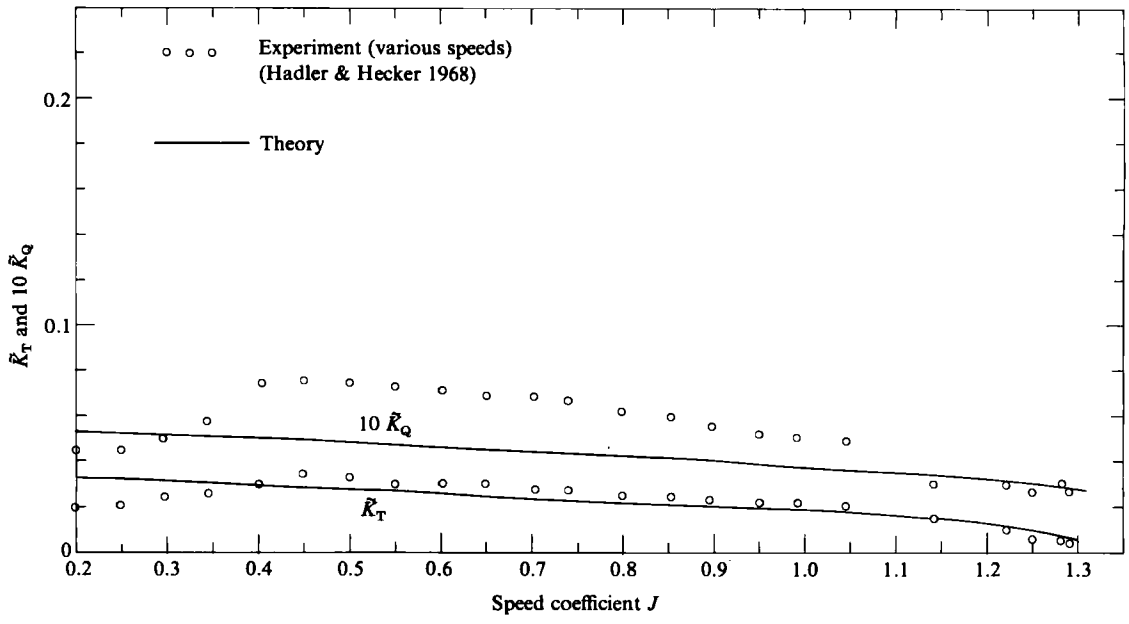

FIGURE 11. Comparison between the present theory and experimental data of Hadler & Hecker (1968) for $\bar{K}_T$ and $\bar{K}_Q$ of propeller model 4002 at submergence 33.3 %.

characteristics of these propellers were given in Hadler & Hecker (1968) who conducted water tunnel tests for these propellers with submerged depth of 40 % and 33.3 %, respectively (the submergence depth was defined with respect to the propeller diameter). Some of the important features used for the present computations are summarized in tables 2 and 3.

The calculated results for the time-averaged thrust and torque coefficients $\bar{K}_T$ and $\bar{K}_Q$ in (58) and (59) are shown in figures 10 and 11 and compared with the experimental data of Hadler & Hecker (1968). The experimental data used in this comparison for Propeller Model 3768 are those with incoming tunnel flow speeds of $U = 10.3$ f.p.s. and 20.7 f.p.s. For $U = 10.3$ f.p.s., much more data than are shown here (particularly beyond $J = 0.6$) are available in their report. However, they indicated that the transition from the leading-edge ventilation to the base-ventilated condition took place at around $J = 0.5$. Since the base-ventilated flow configuration is not of current interest, the data beyond $J = 0.5$ were omitted from the present comparison. On the other hand, for the data taken at $U = 20.7$ f.p.s., there was no indication of such flow transition in the report. It is assumed that the flow configuration matches that of the current theory and all available data are presented. For the propeller model 4002, Hadler and Hecker conducted the experiments with variable incoming speeds and did not indicate the transition point in their data presentation. All experimental data for 4002 are presented for comparison.

In any case the thrust coefficients obtained with the present theory compare favourably with the experimental data over a wide range of J, whereas there exists some discrepancy for the torque coefficients. Various reasons for the discrepancy are considered and can be summarized as follows:

(i) The two-dimensional loadings used in the present calculations are those obtained with Wang's (1979) program which was based on the linearized theory. According

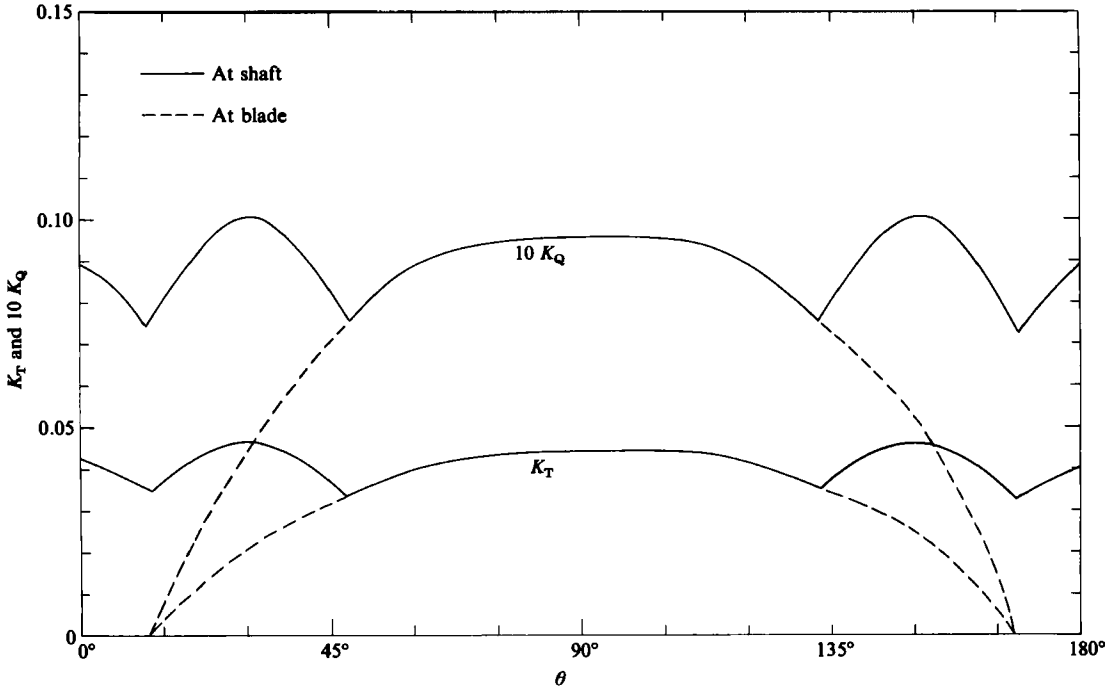

FIGURE 12. Change of thrust and torque coefficients as a function of rotational angle for the propeller shaft and individual blade of model 3768 at submergence of 40 % and $J = 1.0$.

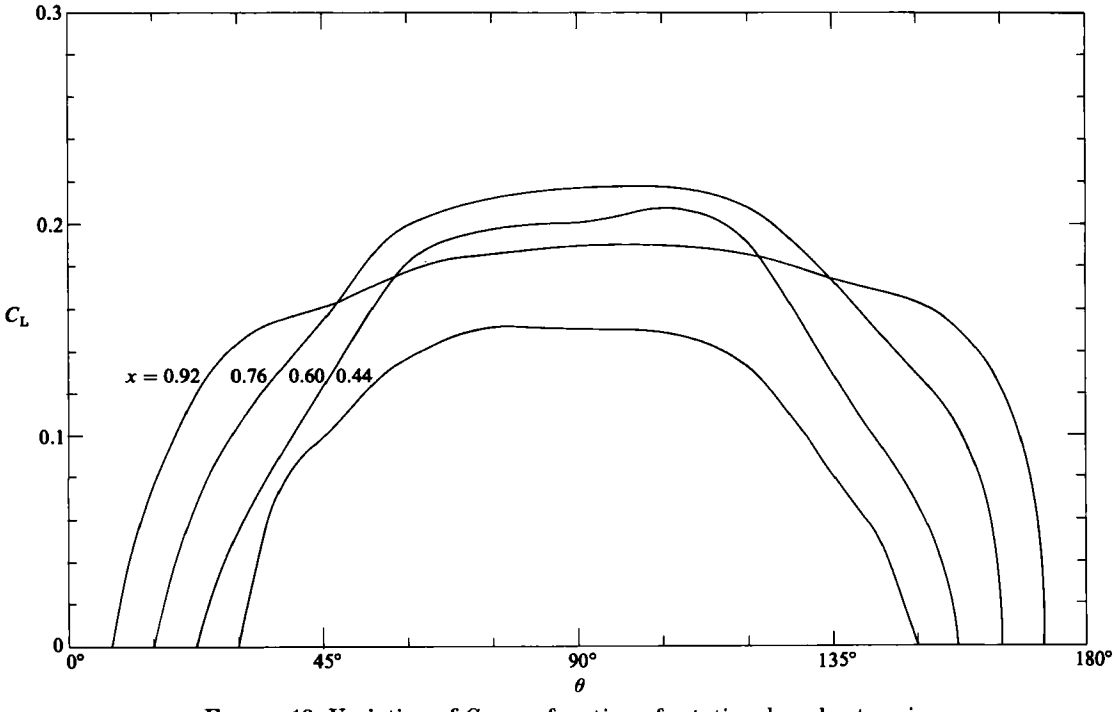

FIGURE 13. Variation of C_L as a function of rotational angle at various blade radial locations for model 3768 at $J = 1.0$.

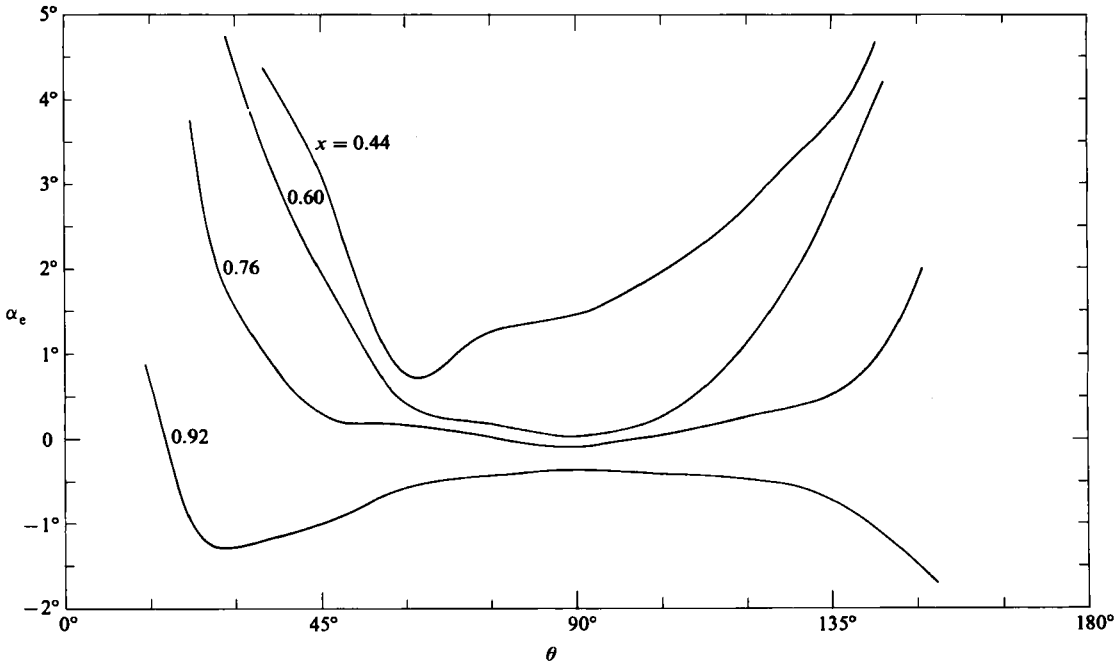

FIGURE 14. Variation of α_e as a function of rotational angle at various blade radial locations for model 3768 at submergence of 40 % and $J = 1.0$.

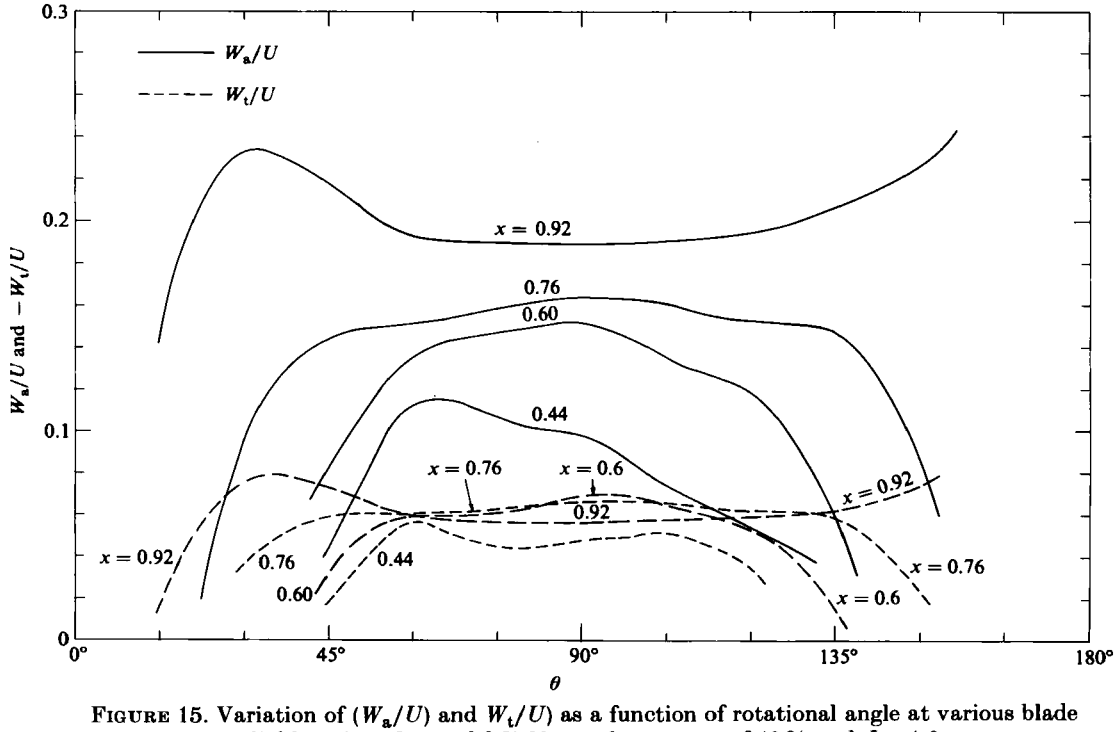

FIGURE 15. Variation of (W_a/U) and $W_t/U)$ as a function of rotational angle at various blade radial locations for model 3768 at submergence of 40 % and $J = 1.0$.

to the recent investigations of D. P. Wang (private communication), the effect of nonlinearity during the phase of blade entry sometimes accounts for 20–30 % of the forces by the linearized theory. This difference may be because the linearized theory is unable to determine the accurate wetted area of the blade during the entry phase.

(ii) In the present computations the pressure doublet terms only were considered in the evaluation of the induced velocities and the pressure source terms were neglected. It has been reported in many documents that the thickness effect of blade or cavity plays an important role in the propeller performance prediction theory (see e.g. Kerwin & Leopold (1963) and Furuya (1980)).

(iii) There exists some uncertainty in interpreting the experimental data, particularly for the case of 4002 as mentioned above. As is seen in figure 11, both $\tilde{K}_T$ and $\tilde{K}_Q$ suddenly increase at around $J = 0.3 \sim 0.4$. There is a suspicion that this behaviour represents the transition from the fully ventilated flow to the base-ventilated flow. If that is the case, the flow configurations of the theory and experiments are not comparable and thus the comparison beyond J of larger than say 0.4 may not be appropriate.

(iv) There exists a limitation of the present lifting-line theory, particularly in the range of small J where the induced velocities become substantial.

Figures 12–15 present the detailed calculated data for 3768 at $J = 1.0$. Figure 12 shows the time-dependent K_T and K_Q as a function of blade rotation. Angle θ of the horizontal axis in this figure is measured from the point when a blade is located at the shaft centreline level. Since propeller 3768 has three blades, the shaft forces are periodic over every 120° of rotation, as is seen from figure 12. The broken lines show K_T and K_Q at each blade, indicating that the water entry point of the blade is about 12° of rotation after the blade passes the shaft centreline.

Figure 13 shows the calculated results of the variation in local lifting forces on the blade at various spanwise points as a function of blade location. Figures 14 and 15 show their corresponding effective flow incidence angles, and the induced velocities, w_a/U and $(-w_t/U)$, respectively. With the information provided in figures 13–15, together with the geometric data shown in table 2, one can readily construct the flow diagram at any location of the propeller model 3768 for $J = 1.0$.

The numerical aspects of the present unsteady propeller problems with the new formula obtained will be discussed in detail in a separate paper in the near future.

7. Conclusions

The purpose of the present work was to develop a mathematical model for solving the time-dependent partially submerged propeller problems and computer program with suitable numerical methods. In the previous work of the author direct integral forms were derived for calculating the induced velocities together with the application of the Hadamard integral method. Unfortunately, this effort resulted in numerical instabilities. Based on the experience encountered there, new mathematical formulae have been successfully developed by converting the fifth-order singularities into third-order singularities. The formulae are similar to those shown by Morgan & Wrench (1965) utilizing the concept of the induction factors (see also the work by Lerbs (1952)). These new formulae are not only applicable to the present partially submerged ventilated propeller problem but also useful for analysing and designing any unsteady subcavitating and cavitating propeller problems, the loading of which does not necessarily have to be periodic.

With the new development of the unsteady propeller lifting-line theory here, the

singular integrals in determining the induced velocities have become numerically stable. By combining the two-dimensional water entry-and-exit theory of Wang (1979), the numerical results have been obtained and compared with the existing experimental data of Hadler & Hecker (1968). It has been found that the overall comparison for K_T is excellent, and that for K_Q is moderate, presumably due to the various power losses such as those of entry and exit splashes and cavity thickness effects, not accounted for in the present method.

This project was supported by the David W. Taylor Naval Ship Research and Development Center of the U.S. Navy, under Contract No. N00167-80-C-0044. The author thanks Dr W. Morgan, Messrs D. Cieslowski and V. Monacella of NSRDC and Dr D. P. Wang for various support.

REFERENCES

Cox, G. G. 1968 Supercavitating propeller theory – The deviations of induced velocity. In *Proc. 7th Symp. on Naval Hydrodynamics, Rome*, pp. 929–960.

Furuya, O. 1980 Off-design performance predictive method for supercavitating propellers. In *Proc. 13th Symp. on Naval Hydrodynamics, Tokyo*, pp. II-2-1–II-2-24.

Hadler, J. B. & Hecker, R. 1968 Performance of partially submerged propellers. In *Proc. 7th Symp. on Naval Hydrodynamics, Rome*, pp. 1449–1496.

Kerwin, J. E. & Leopold, R. 1963 Propeller-incidence correction due to blade thickness. *J. Ship Res.* **7**, 1–6.

Lerbs, H. W. 1952 Modulated loaded propellers with a finite number of blades and an arbitrary distribution of circulation. *SNAME Trans.* **60**, 73–123.

Mangler, K. W. 1951 Improper integrals in theoretical aerodynamics. *RAE, Farnborough, Rep.* Aero 2424.

Morgan, W. B. & Wrench, J. W. 1965 Some computational aspects of propeller design. In *Methods of Computational Physics*, vol. 4, pp. 301–331. Academic.

Monacella, V. J. 1967 On ignoring the singularity in the numerical evaluation of Cauchy principal value integrals. *US Navy NSRDC R & D Rep.* 23–56.

Wang, D. P. 1977 Water entry and exit of a fully ventilated foil. *J. Ship Res.* **21**, 44–68.

Wang, D. P. 1979 Oblique water entry and exit of a fully ventilated foil. *J. Ship Res.* **23**, 43–54.

Yim, B. Y. 1969 Application of linearized theory to water entry and water exit problems. Part 2. With ventilation. *NSRDC Rep.* 3171.

Yim, B. Y. 1971 Investigation of gravity and ventilation effects in water entry of thin foils. In *Proc. IUTAM Symp. Leningrad.*

Yim, B. Y. 1974 Linear theory on water entry and exit problems of a ventilating thin wedge. *J. Ship. Res.* **18**, 1–11.